Low-Frequency Carrier Kinetics in Triple Cation Perovskite Solar Cells Probed by Impedance and Modulus Spectroscopy

Naveen Kumar Tailor[†], Satyaprasad P. Senanayak[‡], Mojtaba Abdi-Jalebi[*,§], Soumitra Satapathi[*,†]

[†]Department of Physics, Indian Institute of Technology Roorkee, Uttarakhand, 247667, India.
[‡] School of Physical Sciences, National Institute of Science Education and Research, HBNI, Jatni, 752050, India.
[§]Institute for Materials Discovery, University College London, Malet Place, London WC1E 7JE, UK.
Email: soumitra.satapath@iitr.ac.in, m.jalebi@ucl.ac.uk

Abstract: Organometallic halide perovskites-based solar cells have emerged as next-generation photovoltaic technology. However, many of its intriguing optoelectronic properties at low frequency are highly debated. Here, we investigate the low-frequency carrier kinetics of the state-of-the-art triple cation perovskite $Cs_{0.06}FA_{0.79}MA_{0.15}Pb(I_{0.85}Br_{0.15})_3$ solar cells using bias-dependent impedance and modulus spectroscopy under dark and illumination conditions. We observe a strong dependence of dielectric permittivity on frequency in 1 Hz to 1 MHz region with a dielectric relaxation, which is observed to follow the Maxwell-Wagner type interfacial polarization possibly originating from the grain boundary/ionic defects. Furthermore, correlating the impedance and modulus spectra reveals the localized charge carrier relaxation in this triple cation device from which we obtain a phenomenological picture of the hopping process and developing an understanding of the charge carrier kinetics in these high-efficiency perovskite photovoltaics.

Keywords: Carrier Kinetics, Triple Cation Perovskite Solar Cells, Impedance, Modulus Spectroscopy

1. Introduction

Perovskite solar cells (PSCs) have reached a power conversion efficiency of over 25% that makes them one of the most promising photovoltaic technology.[1-11] In spite of the exceptional growing interest in the related research, some of the specific photophysical properties of these mixed ionic electronic semiconductors are yet to be explored. Various dielectric spectroscopy studies have speculated the possible existence of ferroelectricity in perovskites. However, in a recent report, a temperature-dependent dielectric and polarization study in $MAPbI_3$ film revealed the non-ferroelectric nature of lead halide perovskites [12]. Although each of these hypotheses and investigation have their own advantages and disadvantage, further studies are necessary to understand the observed hysteresis especially in high-efficiency perovskite solar cells (multi-cationic mixtures compared to conventional $MAPbI_3$) to optimize its design and enhance power conversion efficiency. Several other perplexing and rather debated phenomena regarding electric transport and charge conduction have also been reported in lead halide perovskite especially at low frequencies. Recently, Shen et al. investigated the low-frequency kinetics in $MAPbI_3$ perovskite grown by solution route and hybrid chemical vapor deposition to be thermally activated trapping and de-trapping process [13]. Sangwan et al. showed a current fluctuation in the frequency range of 100-200 Hz with two-hole transport layers, poly-triarylamine (PTAA) and spiro-OMeTAD, and SnO_2 as an electron transport layer [14]. Although several such studies have mainly focused on single cation based mixed halide perovskite solar cells, there are not many reports available in the literature about the photophysical studies of highly efficient and stable perovskite solar cells like the recently reported triple cation mixed halide perovskite solar cells which exhibit rather enhanced stability and efficiency (η ~ 21.1% and stability of 250 hours) [15]. These were further improved upon potassium passivation effect at the grain boundaries in triple cation perovskites by Abdi-Jalebi et al. [16, 17] Therefore, a thorough study and understanding of the fundamental physical processes at low frequency in these triple cation perovskite devices is essential to enable further optimization of the device performance and reach the maximum efficiency in these class of materials. Here, we have utilized these multi-cationic highly efficient perovskites solar cell composition: $Cs_{0.06}FA_{0.79}MA_{0.15}Pb(I_{0.85}Br_{0.15})_3$ as a platform to probe its interesting photophysical properties through a combination of impedance and modulus spectroscopy in the low and intermediate frequency region.

Impedance spectroscopy (IS) has been extensively utilized to probe the charge carrier dynamics in perovskites solar cells [18-21]. Sanchez et al. explained the slow dynamics process in perovskite solar cells with impedance and capacitance spectroscopy [22]. Amalie et al. investigated the effect of changing the concentration of additives in the perovskite hole transport layer with the help of IS spectroscopy [19]. In the triple cation perovskite solar cells, M. Salado et al. revealed the charge generation dynamics and showed the reduced charge carrier recombination at the perovskite/TiO_2 interface by IS spectroscopy [23]. Similarly, IS has also been widely used to probe the recombination dynamics and understand the limiting factors in a photovoltaic device [24]. In addition to IS, correlated modulus spectroscopy is also a useful tool to understand the microscopic mechanism of charge transport, [25-27] relaxation behavior [28] and contribution of the grain boundary in oxide perovskites [29] and to a preliminary extent in these lead halide based hybrid perovskites such as cesium lead bromide ($CsPbBr_3$) [30] and $MAPbI_3$ thin films [25].

Nevertheless, a complete understanding of the relaxation mechanism through a comprehensive study of IS and modulus spectroscopy on a complete device is lagging.

In the present work, we have thus investigated the bias and frequency dependence of the impedance, dielectric relaxation, and electrical modulus phenomenon in triple cation perovskite $Cs_{0.06}FA_{0.79}MA_{0.15}Pb(I_{0.85}Br_{0.15})_3$ solar cells device. We selected the frequency range from lower frequency (1Hz) to higher frequency (1MHz) to investigate the response of carriers (ions and electrons). We have experimentally investigated the trends of real and imaginary impedance, dielectric constant, electrical modulus with frequency in dark, and illumination conditions. Our observation shows that the capacitance and dielectric constant follows the Maxwell-Wagner model, the imaginary part of impedance (Z'') suggests a non-Debye type dielectric relaxation and modulus (M'') peaks correlates to the jump relaxation model for the conductivity dispersion. These observations are important to understand the impedance response and polarization phenomenon in the triple cation perovskite solar cells. Based on the combination of these measurements, we provide a microscopic understanding of the various sources of polarization and conduction mechanisms present in these highly efficient photovoltaic devices.

2. Experimental Section

2.1. Triple-cation perovskite film and device fabrication

Methylammonium bromide (MABr) and Formamidinium iodide (FAI) were purchased from Great Cell Solar Inc., lead iodide (PbI_2) and lead bromide ($PbBr_2$) were purchased from TCI chemicals. Cesium iodide (CsI) was purchased from Alfa Aesar, Spiro-OMeTAD was purchased from Borun Chemicals and used as received. Used solvents were purchased from Sigma-Aldrich. The triple-cation-based perovskite $Cs_{0.06}FA_{0.79}MA_{0.15}Pb(I_{0.85}Br_{0.15})_3$ films were prepared by mixing Lead Iodide $PbI_2(1.2M)$, Methylammonium Bromide (0.21 M), Formamidinium iodide (1.11 M) and Lead Bromide $PbBr_2$(0.21 M) in a mixture of anhydrous DMF: DMSO (4:1 volume ratio, v:v) followed by addition of 5 vol% from CsI stock solution (1.5 M in DMSO) for the synthesis of triple cation perovskite. Then perovskite films were spin-coated from the perovskite solutions using a two-step program at 2,000 and 6,000 rpm for 10 s and 20 s, respectively. 20 seconds after the spinning process, 150 µl drop of chlorobenzene was added and the films were then annealed at 100 °C for 1 h. All the film preparations were performed in a nitrogen-filled glove box. The thickness of fabricated films was measured via cross-sectional SEM (Merlin) and profilometer (Dektak® Profilers - Bruker Nano). The devices were fabricated following the same procedures [16] for perovskite layer preparation as well as deposition of both electron and hole transport layers (that is, TiO_2, spiro-OMeTAD). Finally, metal electrodes (i.e. Au, 80 nm thick) for the devices were coated by thermal evaporation with a chamber pressure of 10^{-6} mbar and an evaporation rate of 0.1 A^0/s. The evaporator system is MBRAUN.

2.2. Optical characterization

Absorption spectra were recorded with an Agilent Cary 100 UV-Vis spectrophotometer equipped with an integrating sphere to account for reflected and transmitted light. Room temperature [25 °C] photoluminescence spectra were taken by a SHIMADZU RF-6000 Spectro Fluorophotometer.

2.3. Electrical characterization

The *I-V* characteristics were measured using the digital source meter (Keithley Model 2400). The 450-W xenon lamp (Oriel) equipped with a Schott-K113 Tempax sunlight filter (Präzisions Glas and OptikGmbH) was used as a light source to match the emission spectrum of the lamp to the AM1.5G standard. Before each measurement, the light intensity was determined using a calibrated silicon reference diode equipped with an infrared cut-off filter (KG-3, Schott) before every measurement. A non-reflective metal aperture of 0.105 cm^2 was used to define the active area of the device and avoid light scattering through the sides. Photocurrent characteristics were measured close to the maximum power point voltage using a Keithley 2636 SMU and a custom-written LabView VI code. IS measurements were recorded using Zahner Electrochemical Workstation in the dark and under illumination (45 mW/cm^2) on completed devices. Measurements were collected for a frequency range of 1 Hz and 1 MHz and at three different bias voltages 50 mV, 100 mV, 200 mV and 300 mV. The equivalent circuit was modeled using ZSimpWin 3.21 software.

3. Results and discussion

Perovskites with ABX_3 structure adopts diverse crystal structures relying on the size and interaction between the A cation and the corner-sharing $[BX_6]^{4-}$ octahedral. In the present work, we endeavor to present a proper stoichiometric ratio of mixed Cs, MA, Br ions into typical $FAPbI_3$ perovskite to acquire stable perovskite phases in the formula of $Cs_xFA_yMA_{(1-x-y)}Pb(I_zBr_{1-z})_3$. The effective radius size of the anion (r_{anion}), cation (r_{cation}), octahedral distortion factor (μ) and effective tolerance factor (t_{eff}) can be assessed by the following equations [31].

$$r_{cation} = xCs + yFA + (1 - x - y)MA \quad \ldots.(1)$$

$$r_{anion} = zI^- + (1 - z)Br^- \quad \ldots.(2)$$

$$\mu = \frac{r_{Pb}}{r_{anion}} \quad \ldots.(3)$$

$$t_{eff} = \frac{r_{cation} + r_{anion}}{\sqrt{2}(r_{Pb}^2 + r_{anion})} \quad \ldots.(4)$$

The ionic radii of FA^+, MA^+, Cs^+, Pb^{2+}, I^- and Br^- are obtained from the literature as follows: 2.53 Å, 2.16 Å, 1.67 Å, 1.02 Å, 2.20 Å and 1.96 Å. As a result, the optimal composition formula with high stability is $Cs_{0.06}FA_{0.79}MA_{0.15}Pb(I_{0.85}Br_{0.15})_3$ with a t_{eff} of 1.01 and μ of 0.47, which falls in the range of 0.8-1.06 and over 0.41, respectively, for a stable perovskite.

The fabricated device structure as per our previously published method [16] with the device architecture: FTO/compact TiO_2 (~30 nm)/thin mesoporous TiO_2 (~200 nm)/perovskite (~500 nm)/Spiro-OMeTAD (~150 nm)/Au (80 nm) is shown in Fig. S3a. Typical absorbance and photoluminescence measurement of the perovskite thin films are shown in Fig. S1. In Fig. S3b, we show the current density versus voltage (*J-V*) characteristics measured with reverse and

forward bias sweeps (dark *J-V* at different scan rates is provided in Fig. S2). J_{sc} = 22.95 mA/cm^2, V_{oc} = 1.12 V and *FF* = 0.78 were obtained from the *J–V* plots, which corresponds to a photoconversion efficiency (PCE) of 20.0 % under AM1.5G condition.

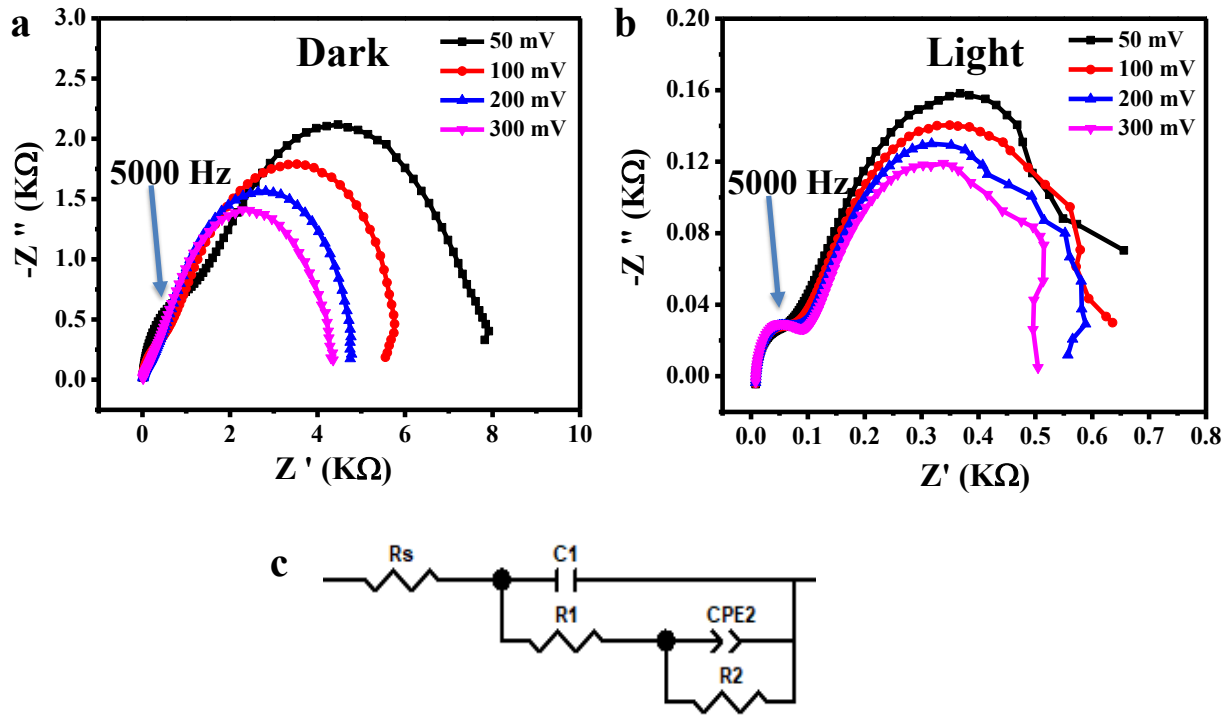

Fig. 1. Impedance spectroscopy characterization of triple cation perovskite solar cell. The behavior of a real and imaginary part of impedance (Nyquist plot) in (a) dark and (b) illumination. (c) The equivalent circuit corresponds to the device, which describes the physical process in the device.

We then measured the impedance response of these stable triple cation perovskite solar cells at different biases in dark as well as under illumination (45 mW/cm^2). Fig. 1a shows the representative Nyquist (Z'-Z'') plots of impedance spectra for triple cation perovskite device under the dark condition with four different bias voltages (50 mV, 100 mV, 200 mV, and 300 mV) in the frequency range of 1 Hz to 1 MHz. We observe that the diameter of the semicircle decreases with higher applied bias, which indicates a reduction of the resistance (R(ω) = Re(Z)) in consistent with the trend observed in the bode plots (Fig. S4). The decrease of the resistance is correlated to an increase of the capacitance in the low-frequency region. Fig. 1b shows the Nyquist plot for devices under illumination condition in the frequency range of 1 Hz to 1MHz range at four different bias voltage. In the Nyquist plot at a higher frequency, we observe a small arc whereas at a lower frequency we observe a large arc. Note that the Nyquist plots do not exhibit a perfectly circular arc, but a depressed semicircle which can be attributed to the deviation from the ideal Debye type charge carrier relaxation process in this triple cation perovskite solar cell [25]. To explain the physical processes taking place in the device, we model the impedance response with an equivalent circuit as shown in Fig. 1c. The fitted results are displayed in Fig. (S9 and S10) and the values of the fitted parameters are shown in Table S1 and S2. In this equivalent circuit, the constant phase

element CPE2 is added with resistance R2 in parallel. The series resistance R_s relates to the ohmic resistance in the device. We calculate the actual capacitance value from CPE2 and R2 and noted it as C2 (Table S1 and S2). The capacitance C2 is associated with the lower frequency region. The capacitance C1 and resistance R1 are related to the intermediate frequency region.

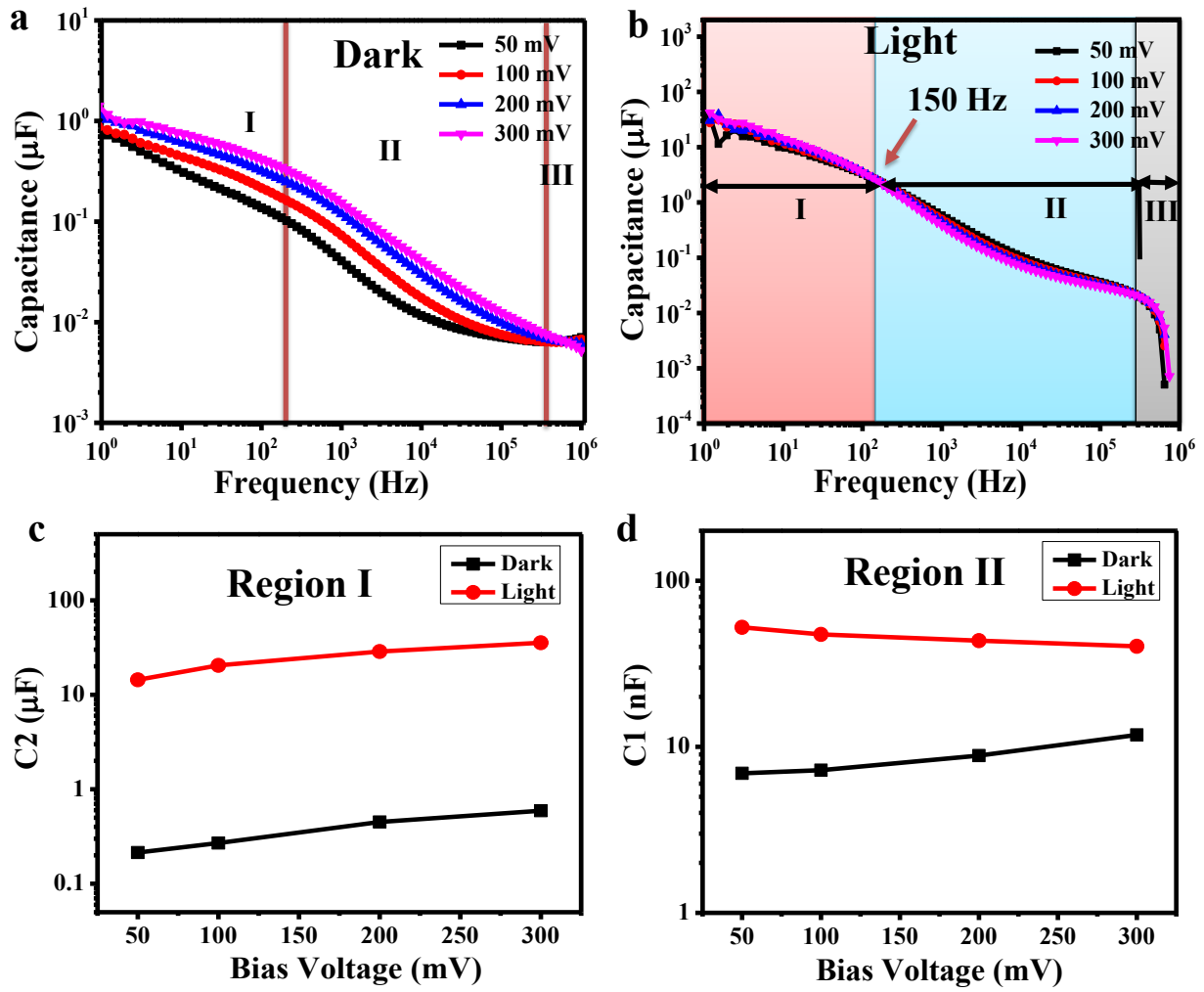

Fig. 2. Capacitance spectrum of a triple cation-based perovskite solar cell with bias at room temperature (a) in dark (b) in light. Capacitance behavior with the bias in both dark and light conditions (calculated from the equivalent circuit). (c) Capacitance C2 with bias in the region I (lower frequency region) and (d) Capacitance C1 with bias in region II (higher frequency region).

The frequency response of the real part of the capacitance (C-f) under dark and light is shown in Fig. 2a and 2b, respectively. We find that both in dark and illumination conditions, the capacitance value is higher in the lower frequency region and it reduces with increasing frequency. This is attributed to the typical polarization relaxation mechanism, wherein with the increase in frequency, different components of polarization are not able to respond to the input frequency thereby decreasing the overall capacitance. However, the bias dependence of capacitance in low frequency and high frequency is different under dark and illumination conditions (Fig. 2a and 2b). To better visualize this, we have marked three different frequency regions namely low-frequency

region (Region I), intermediate frequency region (Region II), and high-frequency region (Region III) in the C-f plots (Fig. 2a and 2b). We calculate the capacitance value from the equivalent circuit model as shown in Fig. 1c and plotted it as a function of bias in Fig. 2c and 2d (more details are provided in Fig. S5). Note that the capacitance C2 in Fig. 2c is associated with region I (lower frequency region) and capacitance C1 in Fig. 2d is related to region II (intermediate frequency region). We observe that the rate of increase of C2 with bias is similar even if the device is measured under dark or illuminated condition. Interestingly we observe a different trend with a bias for C1. Illuminated devices exhibited a negative coefficient for dC1/dV whereas devices measured under dark exhibited a positive coefficient. This transition from positive to negative coefficient with a bias for illuminated devices is observed to be at around 150 Hz which separates region I from region II. Note that such a transition was previously observed in $MAPbI_3$ film (temperature-dependent polarization and dielectric study) where the transition frequency point is ~ 10^3 Hz [12]. In order to further understand this behavior, we measured the variation of the real part of the dielectric constant (ε') with frequency (Fig. 3a and 3b) with different bias voltage at 50 mV, 100 mV, 200 mV, and 300 mV. The high value of dielectric constant at a lower frequency cannot be attributed to the ferroelectric nature [12, 32, 33] but can be attributed to the inherent polar nature of the material triple cation $Cs_{0.06}FA_{0.79}MA_{0.15}Pb(I_{0.85}Br_{0.15})_3$ perovskite. In these types of mixed semiconducting materials, the polar nature originates from multiple polarizations such as orientation, interfacial, and deformational (ionic and electronic) polarization resulting from electronic trapping, molecular dipoles, and ionic accumulation. Thus, in the presence of a time-reversal alternating field, the polarization contributions from various factors decrease thereby resulting in a descending trend of ε'. This type of dielectric relaxation nature can be understood using Koop's theory, in which triple cation perovskite $Cs_{0.06}FA_{0.79}MA_{0.15}Pb(I_{0.85}Br_{0.15})_3$ is treated as an inhomogeneous medium consisting of two Maxwell-Wagner type layers. In this model, the material is assumed to be composed of conducting grain separated by poorly conducting grain boundary [34, 35]. The electronic polarization (high-frequency regime: Region III) originates from the accumulation of electrons at the grain boundaries. In addition to the electronic polarization, the triple cation perovskite: $Cs_{0.06}FA_{0.79}MA_{0.15}Pb(I_{0.85}Br_{0.15})_3$ crystal also contains Cs^+, MA^+, FA^+, Pb^{2+}, I^- and Br^- ions which contribute to the ionic polarization in the material with a low-frequency relaxation (Region I). This is confirmed from the dielectric loss spectroscopy: ε"(f) in our perovskite device shows a typical $1/f^{\gamma}$ behavior (in the low-frequency regime) where the γ is 0.95 (Fig. S6) in consistent with the Jonscher's power law that reveals significant ionic conductivity [33, 36]. In addition to this, the intermediate frequency regime (Region II) is majorly dominated by the polarization originating from the MA^+ and FA^+ dipoles. Considering the contribution of the above factors to the overall dielectric constant, it is expected that the dielectric constant should increase with an increase in bias (Fig. 3a) for samples measured under dark over the whole frequency regime. However, when the dielectric constant is measured under illumination, the

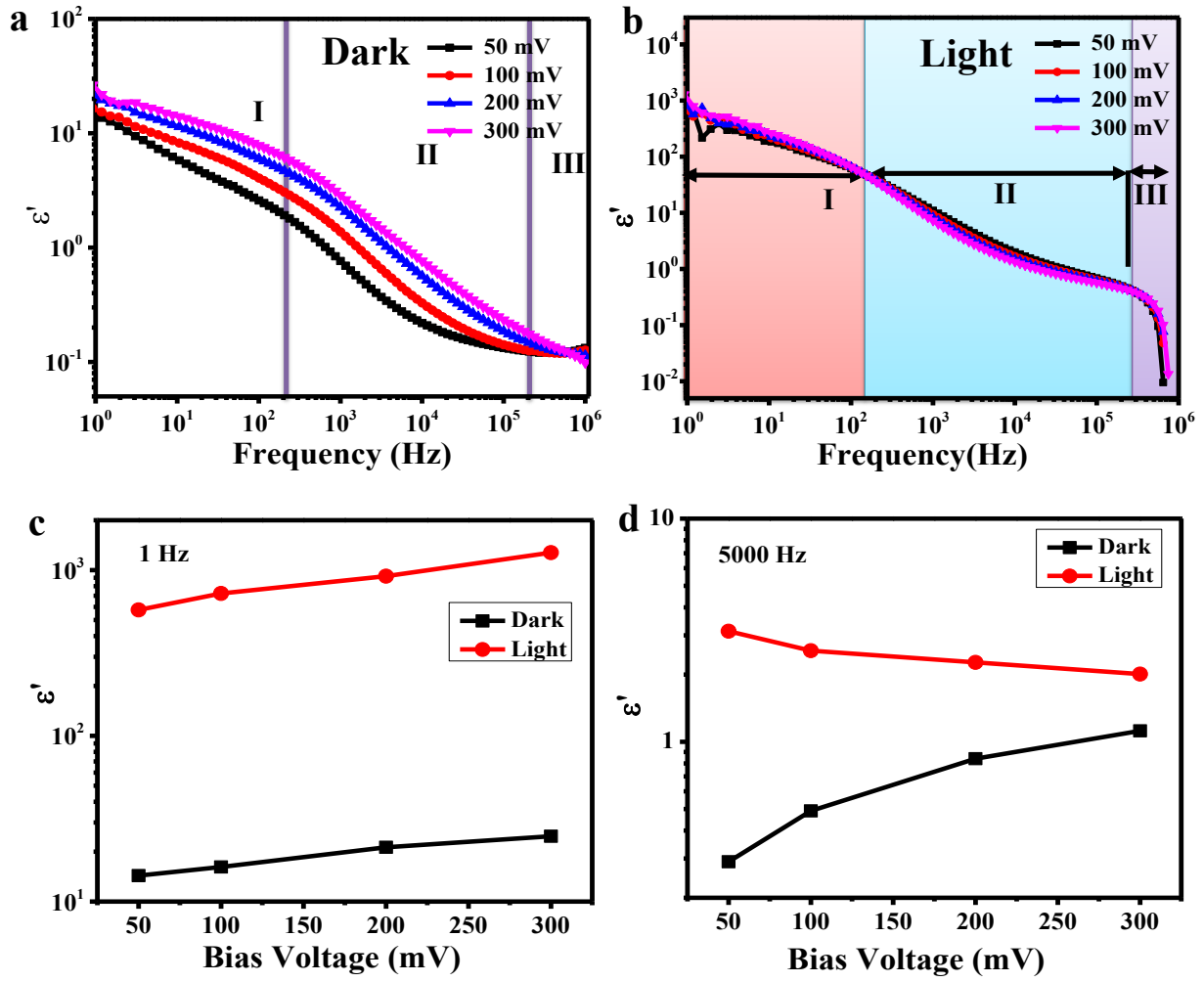

Fig. 3. Real part of dielectric constant variation with frequency of triple cation perovskite solar cell at different applied bias (50 mV, 100mV, 200 mV and 300 mV) at room temperature (a) in dark (b) under illumination. Variation of ε' with bias when the devices were measured under dark and illumination condition at frequency (c) 1 Hz and (d) 5000 Hz.

variation in dielectric constant with bias is not significant (Fig. 3b). The dielectric constant variation with bias is shown in Fig. 3c and 3d. For devices measured under illumination, ε'exhibits an increase with an increase in bias voltage in the low-frequency regime (Region I) due to the bias-induced ionic migration in perovskites. This behavior is consistent with the results shown in Fig. 2c. Interestingly, in the intermediate frequency range (Region II) the variation of ε' with bias exhibits the opposite trend when the devices were measured under illumination and under dark. In region II, ε' is predominantly contributed by the polarization of the cationic dipoles (MA^+, FA^+). When devices are measured in dark, the bias dependent ε'increases due to improved alignment of molecular dipoles. However, when the same measurement is performed on the device under illumination a decreasing trend of dielectric constant is observed. This could possibly be explained by the competing effect of photo-induced lattice expansion leading to increased entropy of the dipoles and bias-induced alignment of molecular dipoles (Fig. 2d and 3d) [37].

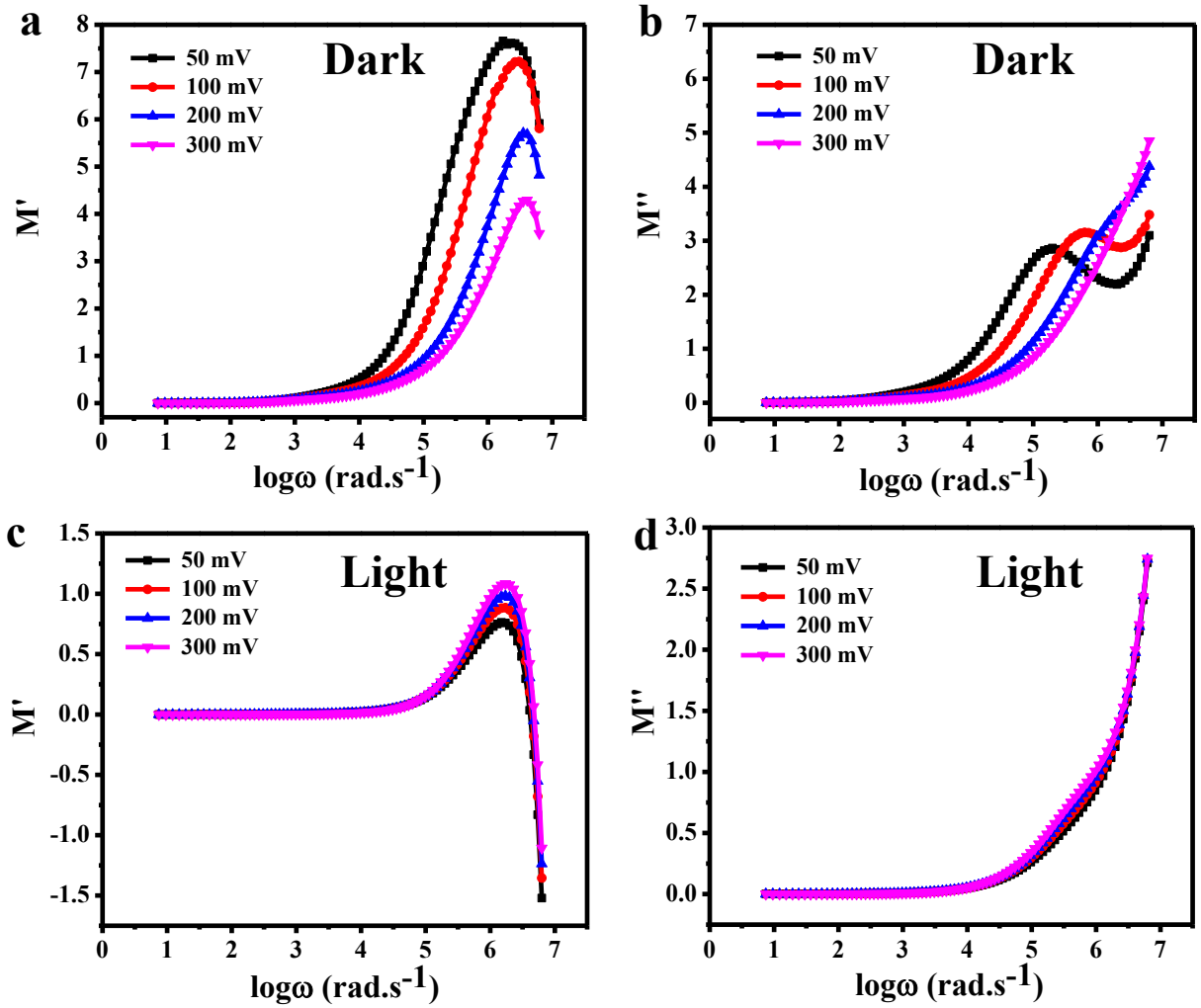

Fig. 4. Frequency dependence of modulus parameters (a) real part of modulus in dark, (b) imaginary part of modulus in dark, (c) real part of modulus in light, (d) imaginary part of modulus in light.

The electric modulus of a sample physically corresponds to the relaxation of the electric field in the material. The complex electric modulus is formulated as [29, 38, 39].

$$M^*(\omega) = \frac{1}{\varepsilon^*} = \frac{1}{\varepsilon' - j\varepsilon''} = \frac{\varepsilon'}{\varepsilon'^2 + \varepsilon''^2} + \mathrm{j}\frac{\varepsilon''}{\varepsilon'^2 + \varepsilon''^2} = M'(\omega) + jM''(\omega) = j\omega C_0 Z^* \quad \ldots.(5)$$

Fig. 4 shows the typical M*(ω) behavior of the triple cation perovskite photovoltaic cells measured under dark and illumination. At lower frequencies, M' is independent of the bias voltage and approaches a magnitude close to zero due to very small electrode polarization [25] and increases as a strong function of frequency in the high-frequency regime, due to the conductance phenomena and mobility/hopping of charge carriers [28, 40-42]. In the low-frequency region, the M'(ω) and M''(ω) value close to zero indicates that the applied electric field is not enough to act as a restoring force for the flow of the charge carriers (Fig. 4a-d) [43-46]. Next, we separately analyze the high-frequency behavior of the M'(ω) and M''(ω). When the photovoltaic device is measured in dark condition, we observe a distinctive peak at a higher frequency and find that the M'(ω) peak value is decreasing and shifting towards higher frequency with increased bias (Fig. 4a). The shift towards

higher frequency is rather related to the dipolar alignment under bias. Similarly, under the dark condition the imaginary part of modulus M" also exhibits a trend of the shift in the peak towards higher frequency upon biasing as shown in Fig. 4b. The M'' peak disappears completely at 200 mV and 300 mV because of increased charge carrier accumulation at the interface with the increase of bias. The shifting of the peak to high frequency suggests that dipoles are confined in the potential well (corresponding to the lead halide inorganic cage) and with an increase in bias, the charge carriers gain enough energy to overcome the potential barrier. The variation of the M'(ω) and M''(ω) while the device is illuminated is shown in Fig. 4c and 4d, respectively. Since there is no change in the low-frequency region with bias, therefore we suggest a suppressed electrode polarization in triple cation halide perovskite [25]. At higher frequency, a peak is observed and the peak height is observed to increase with bias in consistent with an increase in dipolar alignment under bias. On the other hand, the imaginary part of modulus follows an exponential increase with a marginal increase of magnitude under bias in consistent with the competing factors of light-induced lattice expansion increasing the entropy of the cationic dipoles and bias induced alignment of dipoles [37].

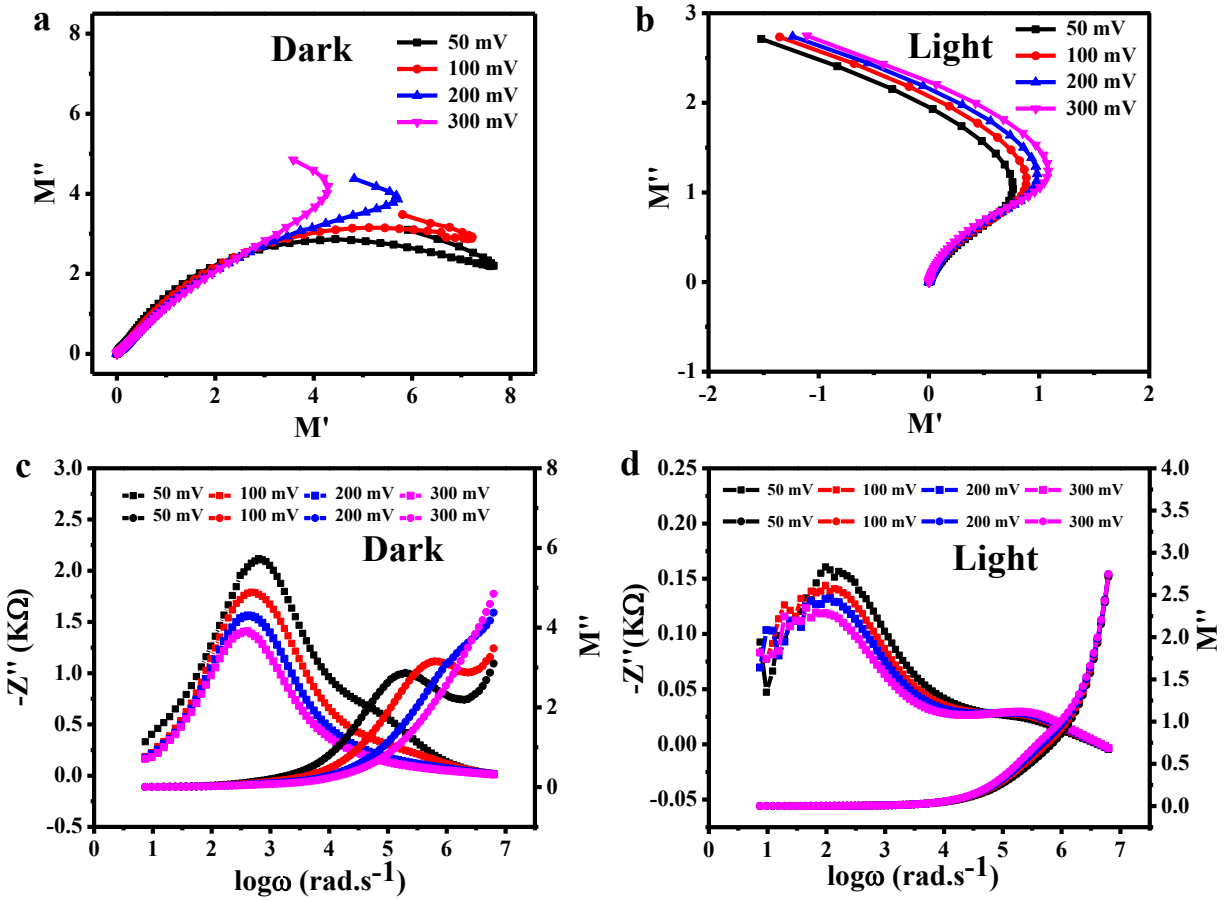

Fig. 5. Modulus Nyquist plot of triple cation perovskite solar cell when the devices were operated under (a) dark (b) light. Z"(ω) and M"(ω) measured on the same device when operated under (c) dark and (d) illumination.

We then plot the room temperature modulus Cole-Cole plot (Fig. 5a and 5b) for the triple cation-based PV devices under dark and illumination conditions, respectively. We find a depressed semicircle in both conditions which confirms the non-Debye type relaxation in the device. At higher frequency, the semicircle turns in the reverse direction, and with increased bias, it is shifted to a lower frequency. In the impedance and correlated electric modulus analysis, the imaginary part of the impedance and electric modulus are plotted as a function of frequency (Fig. 5c and 5d). It is reported that the comparison of impedance with electrical modulus allows determining the bulk response in terms of localized (defect relaxation) or non-localized conduction (ionic or electronic conductivity) [39, 45]. The Debye relaxation model is related to an ideal frequency response of the localized relaxation. In reality, the non-localized process is dominated at the lower frequency region and the nature of dielectric response can be determined by the inspection of the magnitude of overlap between the peaks of both Z″ and M″ [39]. The plot of M" and Z" with frequency distinguishes between the short and long-range movements of charge carriers. The mismatching of $Z"_{max}$ and $M"_{max}$ peaks suggest the short-range flow of charge carriers whereas the matching indicates the long-range type charge carriers. In addition, the peak height in Z"(ω) plot is proportional to the resistance of that process, while the peak height in M"(ω) plot is inversely proportional to the capacitance. In the present case, the low-frequency response is due to the relaxation process of ions, and in the higher frequency region, relaxation is due to the bulk response of perovskite crystals, molecular dipoles, and electronic defect states. We observe that the peak position in the Z″(ω) plot is shifted to a lower frequency region with respect to the peak position in M″(ω) (Fig. 5c and 5d) confirming short-range hopping of charge carrier, localized relaxation, and deviation from ideal Debye-like behavior in the triple cation perovskite photovoltaics [25, 45, 47, 48]. Interestingly, under illumination Z''(ω) exhibits two peaks, a large peak in the lower frequency region and a small peak in the higher frequency region. In the lower frequency region Z''(ω) peak height reduces with the bias in both conditions which suggests the reduction of resistance with bias. The higher frequency Z''(ω) peak increase with the bias and suggests a resistance increase in this region. Correspondingly the M''(ω) peak occurs in the higher frequency region and it increases with bias which suggests the reduction of capacitance with bias in the higher frequency region is consistent with the C(f) behavior as discussed above (Fig. 2). The peak position in each of these plots corresponds to $\omega\tau = 1$ where τ is relaxation time and ω is the frequency corresponding to characteristic relaxation. Typical relaxation time ($\tau_Z \sim 1$ - 2 ms for devices measured under dark and 5 - 12 ms for devices measured under illumination) estimated from the Z" peak position in the dark and light condition is shown in Fig. S7. We observe that τ_Z increases with bias and under illumination indicating the role of bias and illumination on the electronic and ionic re-organization in perovskites [49, 50].

Furthermore, since charge carrier conductivity plays a dominant role in J_{sc} determination, we extracted the conductivity dispersion in triple cation perovskite from the impedance data using the following relation: $\sigma = \frac{t}{A} \frac{Z\prime}{(Z\prime^2 + Z\prime\prime^2)}$, where t is the thickness and A is the area of the device [25, 51-53]. The conductivity plots are shown in (Fig. 6) for PV devices under dark and

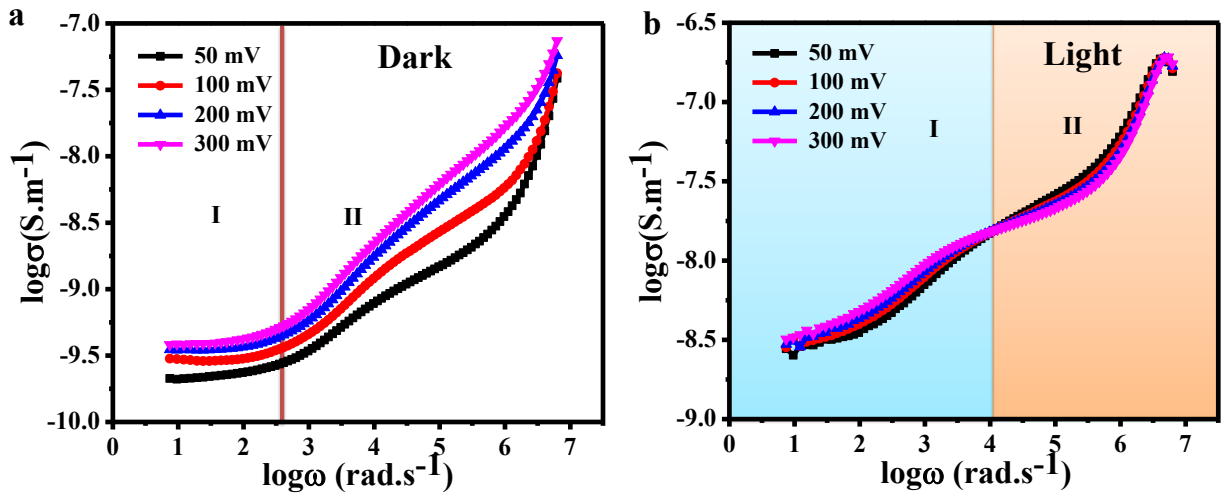

Fig. 6. Logarithmic angular frequency plot of conductivity of triple cation perovskite solar cell derived from impedance data (a) in dark and (b) in light.

illumination exhibits two regimes: low frequency (Region I) which exhibits a conductivity plateau and high frequency (Region II) which exhibits an increase in conduction with frequency. This behavior can be related to the increase in admittance of the capacitor with an increase in frequency. At a microscopic level, the Region I conductivity is approximately equal to the DC conduction due to short-range hopping. Consistent with the JRM the low-frequency electric field is not expected to significantly perturb the hopping conduction mechanism of charge carriers (electrons and holes) and molecular dipoles (MA^+, FA^+) [53, 54]. Upon increasing the frequency, the density of localized charge carriers increases as the non-equilibrium occupancy of the trapped charged carriers decreases resulting in an enhancement in the conductivity of the sample [25, 51]. When bias on the device is increased the admittance further increases (increased ion migration and/or charge carrier conduction with the field) over the complete frequency range, thus resulting in increased conduction over the whole frequency range (Fig. 6a). However, when the devices were measured under the light in the lower frequency region (Region I), the conductivity enhances with the bias voltage and above frequency ~ 2000 Hz (Region II), the conductivity reduces with increased bias (Fig. 6b and S8). This trend is consistent with capacitance and dielectric constant measurement. It is important to note that the bias-dependent increase in the conductivity observed in Region I for devices measured under illumination is marginal. This is because illumination results in ionic redistribution creating [50] a new equilibrium that remains unperturbed with the small bias voltages used in the present experiment. In the high-frequency regime (Region II) the observed decrease in σ with bias may be correlated to the competing nature of photo-induced lattice expansion increasing the entropy of the cationic dipoles [37] and the bias-induced ordering of the molecular dipoles [33, 49]. Both these factors can modify the transport energy landscape due to dipolar disorder resulting in the observed decrease in conductivity. Nevertheless, a detailed understanding of the conductivity dispersion in these PV devices requires further investigation.

4. Conclusions

In summary, we explored the various polarization relaxation mechanisms prevalent in highly efficient perovskite photovoltaics and their impact on charge carrier dynamics through impedance and modulus spectroscopy. The obtained results clearly distinguish the contribution of ionic, molecular, and electronic polarization on the charge carrier kinetics, electrical modulus, and conductivity of the triple cation perovskite photovoltaic device. The dielectric relaxation was observed to follow the Maxwell-Wagner type interfacial polarization and the correlated electric modulus analysis confirms the localized and non-Debye type relaxation with a JRM model for carrier/ionic hopping. Interestingly we observe various competing sources of polarization when the device is illuminated which influences the overall conductivity of the device and the photoconversion efficiency. We believe that this work will help to understand the relaxation behavior in perovskite solar cells and correlate it to the optoelectronic performance of these classes of materials.

Declaration of Competing Interest
The authors declare no conflict of interest.

Credit author statement

Acknowledgments

NKT like to acknowledge UGC Research Fellowship. MA-J thanks Cambridge Materials Limited, the Royal Society (RGS\R1\211068), Wolfson College, University of Cambridge and EPSRC for their funding and technical support. SPS thanks Royal Society Alumni Fellowship, SERB Project (SRG/2020/001641) and DAE Government of India for funding support. SS like to acknowledge Ministry of Electronics and Information technology DIC-1377-PHY.

Supplementary material
Supplementary material associated with this article can be found, in the online version.

References

[1] M. Stolterfoht, M. Grischek, P. Caprioglio, C.M. Wolff, E. Gutierrez-Partida, F. Pena-Camargo, D. Rothhardt, S. Zhang, M. Raoufi, J. Wolansky, M. Abdi-Jalebi, S.D. Stranks, S. Albrecht, T. Kirchartz, D. Neher, How To Quantify the Efficiency Potential of Neat Perovskite Films: Perovskite Semiconductors with an Implied Efficiency Exceeding 28, Adv. Mater. 32 (2020) e2000080.
[2] A. Raghav, S. Singh, D. Moghe, S. Sharma, D. Kabra, S. Satapathi, Charge carrier dynamics study and morphology optimization in solvent annealed CH3NH3PbI3 perovskite for air processed stable solar cell application, Chem. Phys. 526 (2019) 110408.
[3] S. Arya, P. Mahajan, R. Gupta, R. Srivastava, N.K. Tailor, S. Satapathi, R.R. Sumathi, R. Datt, V. Gupta, A comprehensive review on synthesis and applications of single crystal perovskite halides, Prog. Solid State Ch. 60 (2020) 100286.

[4] A. Raghav, S. Singh, S.K. Sharma, D. Kabra, M. Bag, S. Satapathi, Controlling morphology of CH3NH3PbI3 perovskite film by dual solvent elimination method, Nano-Struct. Nano Object 12 (2017) 106-112.
[5] N.K. Tailor, P. Maity, M.I. Saidaminov, N. Pradhan, S. Satapathi, Dark Self-Healing-Mediated Negative Photoconductivity of a Lead-Free Cs3Bi2Cl9 Perovskite Single Crystal, J. Phys. Chem. Lett. (2021) 2286-2292.
[6] N.K. Tailor, S. Satapathi, The impact of Cs3Bi2Cl9 single crystal growth modality on its symmetry and morphology, J. Mater. Res. Technol. 9 (2020) 7149-7157.
[7] M. Kumar Chini, S. Goverapet Srinivasan, N.K. Tailor, Yukta, D. Salahub, S. Satapathi, Lead-free, stable mixed halide double perovskites Cs2AgBiBr6 and Cs2AgBiBr6−xClx – A detailed theoretical and experimental study, Chem. Phys. 529 (2020) 110547.
[8] J.K. Wenderott, A. Raghav, M. Shtein, P.F. Green, S. Satapathi, Local Optoelectronic Characterization of Solvent-Annealed, Lead-Free, Bismuth-Based Perovskite Films, Langmuir. 34 (2018) 7647-7654.
[9] N.K. Tailor, S. Satapathi, Photosensitive Dielectric and Conductivity Relaxation in Lead-Free Cs3Bi2Cl9 Perovskite Single Crystals, J. Phys. Chem. C (2021) https://doi.org/10.1021/acs.jpcc.1c00296.
[10] N.K. Tailor, M. Abdi-Jalebi, V. Gupta, H.L. Hu, M.I. Dar, G. Li, S. Satapathi, Recent progress in morphology optimization in perovskite solar cell, J. Mater. Chem. A 8 (2020) 21356-21386.
[11] N.K. Tailor, S. Satapathi, Structural Disorder and Spin Dynamics Study in Millimeter-Sized All-Inorganic Lead-Free Cesium Bismuth Halide Perovskite Single Crystals, ACS Appl. Energy Mater. 3 (2020) 11732-11740.
[12] M.N.F. Hoque, M. Yang, Z. Li, N. Islam, X. Pan, K. Zhu, Z. Fan, Polarization and Dielectric Study of Methylammonium Lead Iodide Thin Film to Reveal its Nonferroelectric Nature under Solar Cell Operating Conditions, ACS Energy Lett. 1 (2016) 142-149.
[13] Q. Shen, A. Ng, Z. Ren, H.C. Gokkaya, A.B. Djurisic, J.A. Zapien, C. Surya, Characterization of Low-Frequency Excess Noise in CH3NH3PbI3-Based Solar Cells Grown by Solution and Hybrid Chemical Vapor Deposition Techniques, ACS Appl. Mater. Interfaces 10 (2018) 371-380.
[14] V.K. Sangwan, M. Zhu, S. Clark, K.A. Luck, T.J. Marks, M.G. Kanatzidis, M.C. Hersam, Low-Frequency Carrier Kinetics in Perovskite Solar Cells, ACS Appl. Mater. Interfaces 11 (2019) 14166-14174.
[15] M. Saliba, T. Matsui, J.Y. Seo, K. Domanski, J.P. Correa-Baena, M.K. Nazeeruddin, S.M. Zakeeruddin, W. Tress, A. Abate, A. Hagfeldt, M. Gratzel, Cesium-containing triple cation perovskite solar cells: improved stability, reproducibility and high efficiency, Energy Environ. Sci. 9 (2016) 1989-1997.
[16] M. Abdi-Jalebi, Z. Andaji-Garmaroudi, S. Cacovich, C. Stavrakas, B. Philippe, J.M. Richter, M. Alsari, E.P. Booker, E.M. Hutter, A.J. Pearson, S. Lilliu, T.J. Savenije, H. Rensmo, G. Divitini, C. Ducati, R.H. Friend, S.D. Stranks, Maximizing and stabilizing luminescence from halide perovskites with potassium passivation, Nature 555 (2018) 497-501.
[17] M. Abdi-Jalebi, Z. Andaji-Garmaroudi, A.J. Pearson, G. Divitini, S. Cacovich, B. Philippe, H. Rensmo, C. Ducati, R.H. Friend, S.D. Stranks, Potassium- and Rubidium-Passivated Alloyed Perovskite Films: Optoelectronic Properties and Moisture Stability, ACS Energy Lett. 3 (2018) 2671-2678.
[18] L. Contreras-Bernal, S. Ramos-Terron, A. Riquelme, P.P. Boix, J. Idigoras, I. Mora-Sero, J.A. Anta, Impedance analysis of perovskite solar cells: a case study, J. Mater. Chem. A 7 (2019) 12191-12200.

[19] A. Dualeh, T. Moehl, N. Tetreault, J. Teuscher, P. Gao, M.K. Nazeeruddin, M. Gratzel, Impedance spectroscopic analysis of lead iodide perovskite-sensitized solid-state solar cells, ACS Nano 8 (2014) 362-373.
[20] A. Zohar, N. Kedem, I. Levine, D. Zohar, A. Vilan, D. Ehre, G. Hodes, D. Cahen, Impedance Spectroscopic Indication for Solid State Electrochemical Reaction in (CH3NH3)PbI3 Films, J. Phys. Chem. Lett. 7 (2016) 191-197.
[21] D. Pitarch-Tena, T.T. Ngo, M. Valles-Pelarda, T. Pauporte, I. Mora-Sero, Impedance Spectroscopy Measurements in Perovskite Solar Cells: Device Stability and Noise Reduction, ACS Energy Lett. 3 (2018) 1044-1048.
[22] R.S. Sanchez, V. Gonzalez-Pedro, J.W. Lee, N.G. Park, Y.S. Kang, I. Mora-Sero, J. Bisquert, Slow Dynamic Processes in Lead Halide Perovskite Solar Cells. Characteristic Times and Hysteresis, J. Phys. Chem. Lett. 5 (2014) 2357-2363.
[23] M. Salado, R.K. Kokal, L. Calio, S. Kazim, M. Deepa, S. Ahmad, Identifying the charge generation dynamics in Cs(+)-based triple cation mixed perovskite solar cells, Phys. Chem. Chem. Phys. 19 (2017) 22905-22914.
[24] M. Xiao, L. Zhao, M. Geng, Y. Li, B. Dong, Z. Xu, L. Wan, W. Li, S. Wang, Selection of an anti-solvent for efficient and stable cesium-containing triple cation planar perovskite solar cells, Nanoscale 10 (2018) 12141-12148.
[25] M.S. Sheikh, A.P. Sakhya, A. Dutta, T.P. Sinha, Dielectric relaxation of CH3NH3PbI3 thin film, Thin Solid Films 638 (2017) 277-281.
[26] M. Abdi-Jalebi, M. Ibrahim Dar, S.P. Senanayak, A. Sadhanala, Z. Andaji-Garmaroudi, L.M. Pazos-Outon, J.M. Richter, A.J. Pearson, H. Sirringhaus, M. Gratzel, R.H. Friend, Charge extraction via graded doping of hole transport layers gives highly luminescent and stable metal halide perovskite devices, Sci. Adv. 5 (2019) eaav2012.
[27] M. Abdi-Jalebi, M.I. Dar, A. Sadhanala, S.P. Senanayak, F. Giordano, S.M. Zakeeruddin, M. Gratzel, R.H. Friend, Impact of a Mesoporous Titania-Perovskite Interface on the Performance of Hybrid Organic-Inorganic Perovskite Solar Cells, J. Phys. Chem. Lett. 7 (2016) 3264-3269.
[28] C.H. Lee, J. Hassan, M. Hashim, R.a.S. Aziz, N.M. Saiden, Complex dielectric modulus and relaxation response at low microwave frequency region of dielectric ceramic Ba6-3xNd8+2xTi18O54, J. Adv. Dielectric. 04 (2014) 1450034.
[29] G.R. Gajula, L.R. Buddiga, K.N. Chidambara Kumar, M. Dasari, Study on electric modulus, complex modulus and conductivity properties of Nb/Sm, Gd doped barium titanate-lithium ferrite ceramic composites, Res. Phys. 17 (2020) 103076.
[30] P. Maji, A. Ray, P. Sadhukhan, S. Chatterjee, S. Das, Study on charge transfer mechanism and dielectric relaxation of cesium lead bromide (CsPbBr3), J. Appl. Phys. 124 (2018) 124102.
[31] Y. Sun, J. Peng, Y. Chen, Y. Yao, Z. Liang, Triple-cation mixed-halide perovskites: towards efficient, annealing-free and air-stable solar cells enabled by Pb(SCN)2 additive, Sci. Rep. 7 (2017) 46193.
[32] J. Beilsten-Edmands, G.E. Eperon, R.D. Johnson, H.J. Snaith, P.G. Radaelli, Non-ferroelectric nature of the conductance hysteresis in CH3NH3PbI3 perovskite-based photovoltaic devices, Appl. Phys. Lett. 106 (2015) 173502.
[33] S.P. Senanayak, B. Yang, T.H. Thomas, N. Giesbrecht, W. Huang, E. Gann, B. Nair, K. Goedel, S. Guha, X. Moya, C.R. McNeill, P. Docampo, A. Sadhanala, R.H. Friend, H. Sirringhaus, Understanding charge transport in lead iodide perovskite thin-film field-effect transistors, Sci. Adv. 3 (2017) e1601935.

[34] A. Radon, D. Lukowiec, M. Kremzer, J. Mikula, P. Wlodarczyk, Electrical Conduction Mechanism and Dielectric Properties of Spherical Shaped Fe(3)O(4) Nanoparticles Synthesized by Co-Precipitation Method, Materials, 11 (2018) 735.
[35] T.T.N. Vu, G. Teyssedre, S.L. Roy, C. Laurent, Maxwell–Wagner Effect in Multi-Layered Dielectrics: Interfacial Charge Measurement and Modelling, Technologies, 5 (2017) 27.
[36] A. Miyata, A. Mitioglu, P. Plochocka, O. Portugall, J.T.-W. Wang, S.D. Stranks, H.J. Snaith, R.J. Nicholas, Direct measurement of the exciton binding energy and effective masses for charge carriers in organic–inorganic tri-halide perovskites, Nat. Phys., 11 (2015) 582-587.
[37] H. Tsai, R. Asadpour, J.C. Blancon, C.C. Stoumpos, O. Durand, J.W. Strzalka, B. Chen, R. Verduzco, P.M. Ajayan, S. Tretiak, J. Even, M.A. Alam, M.G. Kanatzidis, W. Nie, A.D. Mohite, Light-induced lattice expansion leads to high-efficiency perovskite solar cells, Science, 360 (2018) 67-70.
[38] P.L. Deepti, S.K. Patri, R.N.P. Choudhary, P.S. Das, Dielectric, impedance and modulus spectroscopy of Ta-based layered perovskite, Phase Transit., 92 (2019) 642-656.
[39] P. Gupta, L.K. Meher, R.N.P. Choudhary, Structural, dielectric, impedance and modulus spectroscopy of BiLa2TiVO9 ceramic, Appl. Phys. a-Mater., 126 (2020) 1-12.
[40] D.K. Mahato, T.P. Sinha, Electrical impedance and electric modulus approach of double perovskite Pr2ZnZrO6 ceramics, J. Mater. Sci. Mater. El., 24 (2013) 4399-4405.
[41] N.V. Prasad, M.C. Sekhar, G.S. Kumar, Impedance Spectroscopic Studies on Lead Based Perovskite Materials, Ferroelectric, 366 (2010) 55-66.
[42] A. Ray, T. Basu, B. Behera, D.S. Gavali, R. Thapa, S. Vajandar, T. Osipowicz, P. Nayak, Structural, dielectric, electrical properties of Nd doped double perovskite ceramics and variation of density of states upon doping, Mater. Chem. Phys., 239 (2020) 122250.
[43] A. Ahad, M.A. Taher, M.K. Das, M.Z. Rahaman, M.N.I. Khan, Effect of Y substitution on magnetic and transport properties of Ba0.95La0.05Ti1−xYxO3 ceramics, Res. Phys., 12 (2019) 1925-1932.
[44] F. Alresheedi, S. Hcini, M.L. Bouazizi, M. Boudard, A. Dhahri, Synthesis and study of impendence spectroscopy properties of La0.6Ca0.2Na0.2MnO3 manganite perovskite prepared using sol–gel method, Journal of Materials Science: Mater. Electron. 11 (2020) 8248-8257.
[45] M. Coskun, O. Polat, F.M. Coskun, Z. Durmus, M. Caglar, A. Turut, The electrical modulus and other dielectric properties by the impedance spectroscopy of LaCrO3 and LaCr0.90Ir0.10O3 perovskites, RSC Adv., 8 (2018) 4634-4648.
[46] M.G. Smitha, M.V. Murugendrappa, Structural, Electrical, Thermal and Transport Properties of Poly Pyrrole/La0.7Ca0.3MnO3 Perovskite Manganite Nano Composite Studies Above Room Temperature, J. Inorg. Organomet. Polymer. Mater., 30 (2019) 841-858.
[47] B. Mohanty, B.N. Parida, R.K. Parida, Structural and conduction behaviour of (BaSr)0.5TiO3 modified in BFO perovskite, Mater. Chem. Phys., 225 (2019) 91-98.
[48] R. Das, R.N.P. Choudhary, Studies of structural, dielectric relaxor and electrical characteristics of lead-free double Perovskite:Gd2NiMnO6, Solid State Sci., 87 (2019) 1-8.
[49] S.P. Senanayak, M. Abdi-Jalebi, V.S. Kamboj, R. Carey, R. Shivanna, T. Tian, G. Schweicher, J. Wang, N. Giesbrecht, D. Di Nuzzo, H.E. Beere, P. Docampo, D.A. Ritchie, D. Fairen-Jimenez, R.H. Friend, H. Sirringhaus, A general approach for hysteresis-free, operationally stable metal halide perovskite field-effect transistors, Sci. Adv., 6 (2020) eaaz4948.
[50] D.W. deQuilettes, W. Zhang, V.M. Burlakov, D.J. Graham, T. Leijtens, A. Osherov, V. Bulovic, H.J. Snaith, D.S. Ginger, S.D. Stranks, Photo-induced halide redistribution in organic-inorganic perovskite films, Nat. Commun., 7 (2016) 11683.

[51] M. Samiee, S. Konduri, B. Ganapathy, R. Kottokkaran, H.A. Abbas, A. Kitahara, P. Joshi, L. Zhang, M. Noack, V. Dalal, Defect density and dielectric constant in perovskite solar cells, Appl. Phys. Lett., 105 (2014) 153502.
[52] P. Chutia, A. Kumar, Charge-carrier relaxation dynamics and ac conductivity scaling of poly(3,4-ethylenedioxythiophene) nanoparticles, physica status solidi (a), 212 (2015) 2727-2737.
[53] S. Pujaru, P. Maji, P. Sadhukhan, A. Ray, B. Ghosh, S. Das, Dielectric relaxation and charge conduction mechanism in mechanochemically synthesized methylammonium bismuth iodide, J. Mater. Sci. Mater. El., 31 (2020) 8670-8679.
[54] W. Tress, Metal Halide Perovskites as Mixed Electronic-Ionic Conductors: Challenges and Opportunities-From Hysteresis to Memristivity, J. Phys. Chem. Lett., 8 (2017) 3106-3114.